The Astrophysical Journal Letters, 921:L27 (6pp), 2021 November 10 https://doi.org/10.3847/2041-8213/ac31a9

A Candidate Kiloparsec-scale Quasar Pair at $z = 5.66$

Minghao Yue, Xiaohui Fan, Jinyi Yang[1], and Feige Wang[2]
Steward Observatory, University of Arizona, 933 North Cherry Avenue, Tucson, AZ 85721, USA; yuemh@email.arizona.edu
Received 2021 September 10; revised 2021 October 16; accepted 2021 October 19; published 2021 November 4

Abstract

We report the discovery of a close quasar pair candidate at $z = 5.66$, J2037–4537. J2037–4537 is resolved into two quasar images at the same redshift in ground-based observations. Follow-up spectroscopy shows significant differences in both the continuum slopes and emission line properties of the two images. The two quasar images have a projected separation of 1.″24 (7.3 kpc at $z = 5.66$) and a redshift difference of $\Delta z \lesssim 0.01$. High-resolution images taken by the Hubble Space Telescope do not detect the foreground lensing galaxy. The observational features of J2037–4537 strongly disfavor the lensing hypothesis. If J2037–4537 is a physical quasar pair, it indicates a quasar clustering signal of $\sim 10^5$ at a separation of ~ 10 proper kpc (pkpc), and gives the first observational constraint on the pair fraction of $z > 5$ quasars, $f_{\rm pair}(r < 30\,{\rm pkpc}) > 0.3\%$. The properties of J2037–4537 are consistent with those of merger-triggered quasar pairs in hydrodynamical simulations of galaxy mergers.

Unified Astronomy Thesaurus concepts: Quasars (1319); Double quasars (406)

1. Introduction

Galaxy mergers are natural consequences of hierarchical structure formation of the universe (e.g., Cole et al. 2000). It has been proposed that galaxy mergers can trigger powerful quasar activity, which regulates the star formation of their host galaxies by significant feedback (e.g., Di Matteo et al. 2005). In some rare cases, the supermassive black holes (SMBHs) in both progenitor galaxies are ignited by the merging event, forming a close pair of quasars (for a recent review, see De Rosa et al. 2019). High-resolution hydrodynamical simulations suggest that close quasar pairs correspond to a special, short-lived phase of galaxy mergers, which most frequently appear when the SMBHs have a mass ratio close to one and a separation smaller than 10 kpc (e.g., Capelo et al. 2015, 2017). Quasar pairs are also predicted in cosmological simulations (e.g., Steinborn et al. 2016; Volonteri et al. 2016; Rosas-Guevara et al. 2019; Di Mascia et al. 2021), and their statistics (e.g., the fraction of pairs among all quasars) constrain the evolution of SMBHs and their host galaxies. In addition, close quasar pairs trace overdensities (e.g., Onoue et al. 2018), and are unique probes of the small-scale structure of intergalactic medium (e.g., Rorai et al. 2017).

Searches of quasar pairs have been carried out using wide-area optical and infrared (IR) sky surveys (e.g., Hennawi et al. 2010; Silverman et al. 2020). These studies have discovered several tens of close quasar pairs (with projected separation $\Delta d \lesssim 10$ kpc) out to $z \sim 3$ (e.g., Shen et al. 2021; Tang et al. 2021). Due to the rapid decline of quasar number densities (e.g., Kulkarni et al. 2019) and the relatively poor physical resolution for most observations, it becomes difficult to identify close quasar pairs at $z \gtrsim 3$. Finding high-redshift quasar pairs is critical to the understanding of the evolution and environment of high-redshift quasars and galaxy mergers.

In this Letter, we report a close quasar pair candidate at redshift $z = 5.66$ with a projected proper distance of $\Delta d = 7.3$ kpc, J2037–4537. Following Hennawi et al. (2010), in this Letter, we define a quasar pair as two quasars with $\Delta d < 1$ Mpc and a radial velocity difference of $\Delta v < 2000\,{\rm km\,s^{-1}}$. We further define close quasar pairs to be those with $\Delta d < 10$ kpc. The most distant quasar pair previously known is at $z = 5.1$ with $\Delta d = 135$ kpc (McGreer et al. 2016), and for close quasar pairs, the highest-redshift one is at $z = 3.1$ with $\Delta d = 7.4$ kpc (Tang et al. 2021). J2037–4537 significantly extends the frontier of studies of quasar pairs.

This Letter is organized as follows. We describe the ground-based observations and the Hubble Space Telescope (HST) imaging in Section 2. We discuss the interpretation of the data in Section 3 and summarize in Section 4. We use a flat ΛCDM cosmology with $H_0 = 70\,{\rm km\,s^{-1}\,Mpc^{-1}}$ and $\Omega_M = 0.3$.

2. Data and Analysis

2.1. Ground-based Imaging and Spectroscopy

J2037–4537 was discovered in our ongoing survey for high-redshift gravitationally lensed quasars (M. Yue et al. 2021, in preparation) in the Dark Energy Survey (DES; e.g., Abbott et al. 2018) field. It is not detected in the DES g band, and has DES $r = 22.8$, $i = 20.4$, $z = 19.6$, and $Y = 19.5$, exhibiting typical colors of a quasar at redshift $z \gtrsim 5.5$ (e.g., Yang et al. 2019). In the DES images (Figure 1, upper left), J2037–4537 appears to be two point sources separated by 1.″24, where the fainter one (object B) is redder than the brighter one (object A). Table 1 lists the photometric properties of the two objects. The magnitudes are obtained by fitting the images as two point sources using *galfit* (Peng et al. 2002), where the point-spread function (PSF) models are built by the IRAF task `psf`.

The optical spectrum of J2037–4537, taken by the Low Dispersion Survey Spectrograph (LDSS-3) on the Magellan/Clay telescope, reveals that both objects are quasars at redshift $z = 5.66$ (Figure 1). We use the VPH-Red grism and the 1.″0 slit, which deliver a resolution of $R = 1350$. The spectrum is

[1] Strittmatter Fellow.
[2] NHFP Hubble Fellow.

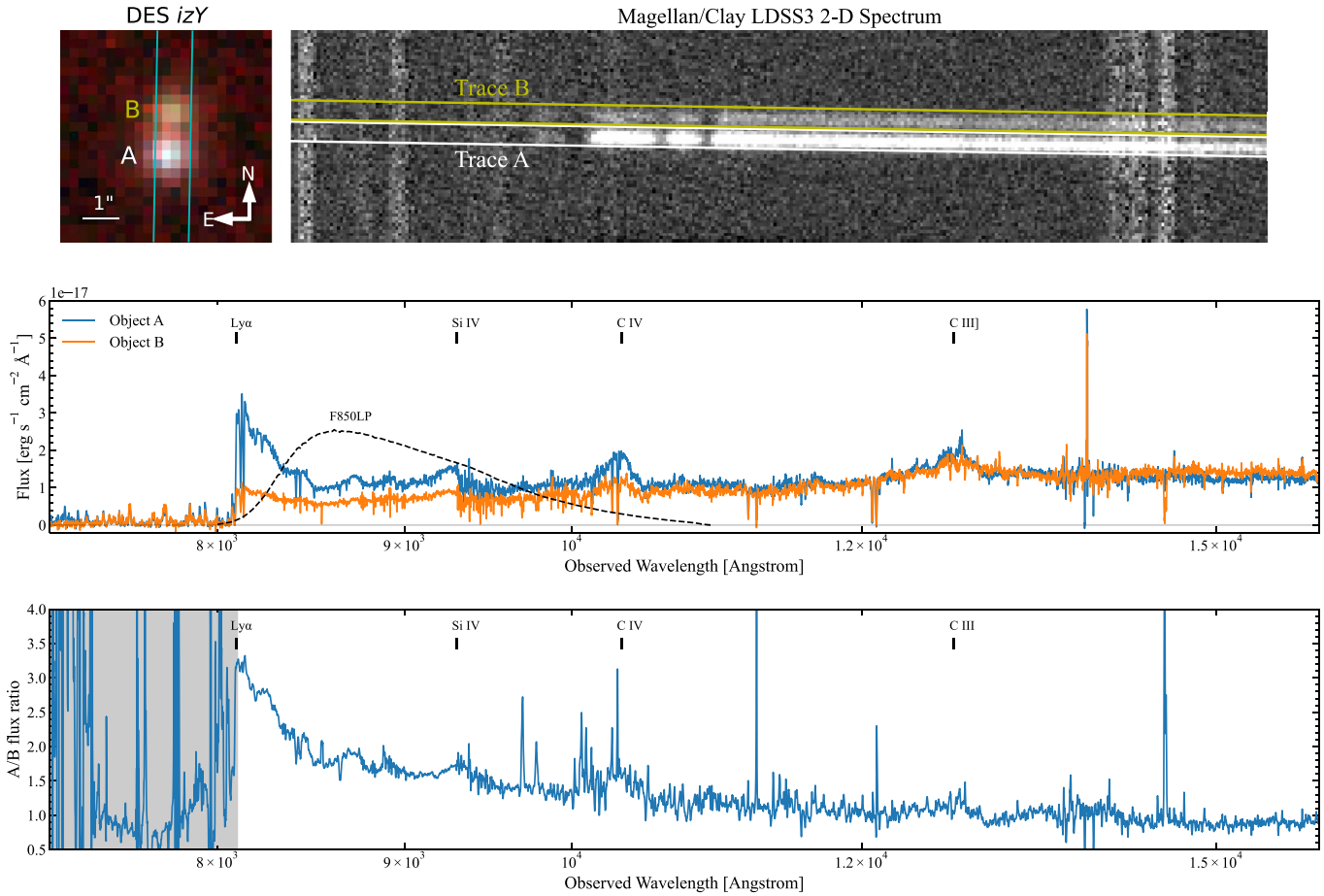

Figure 1. Ground-based imaging and spectroscopy of J2037–4537. Upper left: the DES *izY* images shown in RGB format. The PSF FWHM of the image is $\sim 0\farcs9$. The fainter component (object B) is redder than the brighter one (object A). The two objects are separated by $1\farcs24$. The cyan lines mark the slit position in the spectroscopy. Upper right: the 2D spectrum taken by Magellan/Clay LDSS-3. The two objects are well-resolved under a seeing of $\sim 0\farcs7$, allowing us to extract the two traces accurately. The white and yellow lines mark the apertures used to extract the 1D spectrum. The Magellan/Baade FIRE spectrum has a better seeing of $\sim 0\farcs6$. Middle panel: the extracted 1D spectrum of the two objects, which is a combination of the Magellan/Clay LDSS-3 spectra ($\lambda < 1$ μm) and the Magellan/Baade FIRE spectra ($\lambda > 1$ μm). Both objects exhibit features of a $z = 5.66$ quasar, and object B is redder than object A. The dashed line shows the F850LP filter used in HST ACS/WFC imaging. Lower panel: the flux ratio between the two objects. The shaded area marks wavelengths bluer than the Lyα break, where the quasars have little flux due to the IGM absorption. There are complex features around the emission lines, which suggest that the two objects have different line profiles, and disfavor the strong-lensing hypothesis.

reduced with the standard IRAF pipeline. The two objects are clearly resolved in the spectrum and have the same Lyα-break wavelength, suggesting a redshift difference $\Delta z \lesssim 0.01$. Object B has a redder spectral energy distribution (SED) shape than object A, which agrees with the broadband photometries. We also obtained near-IR spectra of the two objects using the Folded-port InfraRed Echelle (FIRE) on Magellan/Baade telescope. The spectra are reduced with `PypeIt` (Prochaska et al. 2020).

J2037–4537 could either be a physical quasar pair, or two images of a strongly lensed quasar. Both the image and the spectra do not show signs of a third object (e.g., a foreground lensing galaxy). This is further confirmed by the HST image (Section 2.2). In addition, the two objects have different emission line profiles. The difference is the most obvious for the C III] line and can also be seen in the A/B flux ratio (Figure 1, lower panel). These features disfavor the strong-lensing scenario and indicate that J2037–4537 is a physical quasar pair.

Figure 2 illustrates the C IV broad emission lines of the two objects, which are fitted as a power-law continuum plus a Gaussian profile. Using the C IV line width and the empirical relation in Vestergaard & Peterson (2006), we estimate the SMBH masses to be $\log M_{\rm BH}/M_\odot = 8.60$ for quasar A and $\log M_{\rm BH}/M_\odot = 8.45$ for quasar B. Although the Mg II line is a better SMBH mass indicator for high-redshift quasars, it falls in the wavelengths with strong sky emission lines at $z = 5.66$. The results are listed in Table 1.

2.2. HST Imaging

Gravitational lensing can also generate two close quasar images at the same redshift. To fully explore the lensing hypothesis, we observed J2037–4537 using HST ACS/WFC in the F850LP filter, aiming at detecting or ruling out the foreground lensing galaxy (Program GO-16507). The F850LP filter has a wavelength coverage of $0.8\,\mu{\rm m} < \lambda < 1.1\,\mu{\rm m}$, where the two objects show significantly different SEDs in the ground-based spectroscopy. Figure 3 presents the HST image and the two-PSF fitting residual. J2037–4537 is well-described by the two-PSF model and there is no evidence for a third object in this field.

To further set a flux limit for the possible lensing galaxy, we measure the flux in the region between the two point sources

Table 1
Properties of J2037–4537

Object	A	B
R.A.	20:37:21.27	−45:37:48.8
Decl.	20:37:21.26	−45:37:47.5
	Magnitudes[a]	
DES g	>25.1	>25.1
DES r	23.09 ± 0.04	24.8 ± 0.2
DES i	20.84 ± 0.01	21.80 ± 0.02
DES z	20.17 ± 0.01	20.67 ± 0.01
DES Y	20.07 ± 0.03	20.39 ± 0.05
F850LP	20.10 ± 0.01	20.67 ± 0.02
	Luminosities	
M_{1450}[b]	−26.42	−25.99
$\log L_{\rm bol}$(erg s^{-1})[c]	47.1	46.9
	C IV line	
$z_{\rm C\,IV}$	5.643 ± 0.002	5.636 ± 0.003
FWHM (km s^{-1})	1967 ± 76	1891 ± 147
$\log M_{\rm BH,C\,IV}(M_\odot)$[d]	8.60	8.45

Notes.
[a] All magnitudes are AB magnitudes. Detection limits are 5σ.
[b] The absolute magnitude at rest frame 1450 Å.
[c] Calculated based on M_{1450} and the bolometric correction in Runnoe et al. (2012).
[d] The SMBH mass based on the relation in Vestergaard & Peterson (2006). The intrinsic scatter of the relation is 0.36 dex, which dominates the uncertainties.

(region C, marked by the red circle in the right panel of Figure 3). Since PSF models of ACS/WFC usually have nonnegligible errors in PSF wings (Jee et al. 2007), we measure two additional regions (C1 and C2, marked by the yellow circles) to correct this systematic uncertainty. The yellow regions have the same size as the red one, and the distance from region C1 (C2) to object A (B) is equal to the distance from region C to object A (B). The flux in region C1 (C2) thus estimates the contribution of the PSF wing residuals from object A (B) to the flux in region C. We estimate the flux of the possible foreground galaxy as

$$F_{\rm foreground} = F_{\rm C} - F_{\rm C1} - F_{\rm C2}. \quad (1)$$

This gives a nondetection and rules out the existence of a foreground lensing galaxy with $m_{\rm F850LP} < 26.7$ at the 3σ level. Assuming a typical redshift of $z_l \sim 1$ for the lensing galaxy (e.g., Hilbert et al. 2008; Wyithe et al. 2011), this limit gives an absolute magnitude of $M \gtrsim -17.6$, which is about four magnitudes fainter than the breaking magnitude of the galaxy luminosity function at $z \sim 1$ ($M_* \sim -21.5$; e.g., Faber et al. 2007).

2.3. Testing the Strong-lensing Hypothesis

The distinct SEDs of the two quasar images and the nondetection of the lensing galaxy strongly disfavor the lensing hypothesis. Although microlensing and/or differential reddening can lead to different spectral features in lensed quasar images (e.g., Sluse et al. 2012), it is difficult for these effects to explain the observational features of J2037–4537. If objects A and B are lensed images of the same quasar, the extinction of image B must be much stronger than A given their colors. At long wavelengths ($\lambda_{\rm obs} \gtrsim 1.5\,\mu$m), image B is brighter than image A, meaning that image A is intrinsically fainter. Meanwhile, in most galaxy-scale lensing systems, the fainter

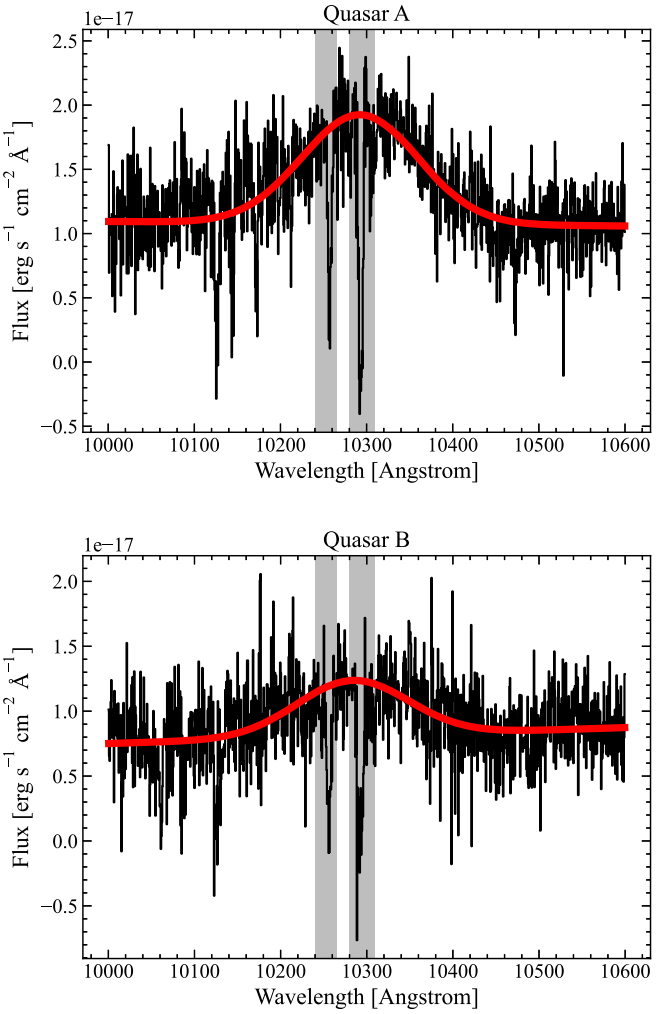

Figure 2. The C IV emission lines of the two quasars (black) and the best-fit model (red). We use a power-law continuum and a Gaussian profile to describe the emission lines. The absorption features (gray dashed area) are masked during the fitting.

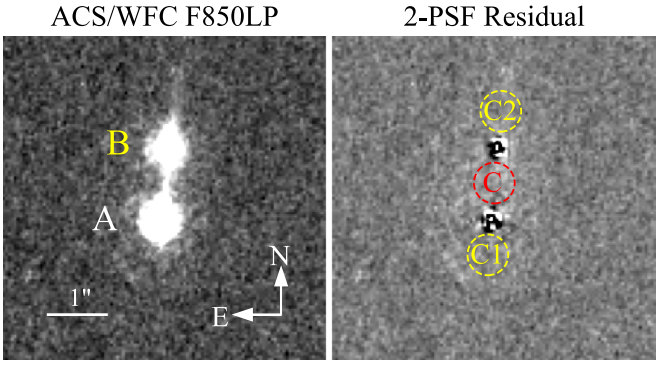

Figure 3. The HST ACS/WFC F850LP image of J2037–4537 (left) and the residual of the two-PSF model (right). There is no sign of a third object besides the two point sources. We measure the flux in area C (the red circle, with a radius of 0.″35) to estimate the flux limit of the possible foreground lensing galaxy. We also measure the fluxes in two additional areas, C1 and C2 (yellow circles), which correct the contributions from the PSF-subtraction residual (see the text for details). Our estimation gives a 3σ flux limit of $m_{\rm F850LP} > 26.7$ for region C.

image is closer to the deflector (e.g., Mason et al. 2015) and should have a stronger extinction. This conflicts with the fact that image B is redder than A, suggesting that the lensing scenario is unlikely.

In principle, a deflector galaxy with highly irregular mass profiles and/or dust distributions might be able to generate a lensing system like J2037–4537. We thus report J2037–4537 as a high-confidence close quasar pair candidate. The definitive test of the lensing scenario can be achieved with the Atacama Large Millimeter/submillimeter Array (ALMA). ALMA will measure the [C II] redshifts of the two quasar images to an accuracy of <0.001 (e.g., Decarli et al. 2018), and will reveal the lensed arcs of the quasar host galaxy. In the following discussions, however, we will treat J2037–4537 as a physical quasar pair.

3. Discussion

3.1. The Pair Fraction of High-redshift Quasars

J2037–4537 has a projected separation of 1.″24 (7.3 kpc at $z = 5.66$). Kiloparsec-scale quasar pairs are rare especially at high redshift, due to the quick decline of the number density of high-redshift quasars. De Rosa et al. (2019) summarize a number of predictions of the active galactic nuclei (AGNs) pair fractions (e.g., Steinborn et al. 2016; Volonteri et al. 2016; Rosas-Guevara et al. 2019). These studies use large-volume cosmological simulations like Magneticum,[3] EAGLES (Schaye et al. 2015), and Horizon-AGN (Dubois et al. 2014), which model the SMBH growth and AGN activities using analytical relations. These studies then count close SMBH pairs that have bolometric luminosities beyond a certain threshold. Specifically, De Rosa et al. (2019) consider AGNs with bolometric luminosity $L_{\rm bol} > 10^{43}\,{\rm erg\,s^{-1}}$, and count AGN pairs with a separation of $r < 30$ proper kpc (pkpc). The predicted pair fraction, $f_{\rm pair}(r < 30\,{\rm pkpc})$, is about 1% with little redshift evolution.

J2037–4537 allows us to constrain the quasar pair fraction at high redshift for the first time. This is done by estimating the expected number of quasars we can find in our survey. J2037–4537 is discovered serendipitously in our survey for high-redshift lensed quasars in the DES field, which covers ~5000 deg^2. We identify J2037–4537 as a lens candidate with quasar-dominated flux, for which we request a nondetection in DES $-$ g, a DES $-$ z magnitude of $m_z < 21$, and a projected separation of $\Delta d < 3.''0$. The g- and z-band flux cuts restrict our targets to $5 \lesssim z \lesssim 6$ quasars (e.g., Wang et al. 2016; Yang et al. 2017, 2019). As the survey is not completed yet, we simply assume a selection function of one for $5 < z < 6$ quasars, and provide the lower limit of the quasar pair fraction.

We use SIMQSO (McGreer et al. 2013) to generate a mock catalog of quasars in the DES field at $5 < z < 6$ that are brighter than $m_z = 21$. SIMQSO is a Python-based package, which generates mock catalogs of quasars with simulated spectra, and has been shown to accurately reproduce the observed colors and magnitudes of quasars (e.g., Ross et al. 2013). We use a broken power law to parameterize the quasar luminosity function (QLF):

$$\Phi = \frac{\Phi^*}{10^{0.4(M-M^*)(\alpha+1)} + 10^{0.4(M-M^*)(\beta+1)}}. \quad (2)$$

[3] http://www.magneticum.org/index.html

We adopt the $z = 5$ QLF from Kim et al. (2020) and the $z = 6$ QLF from Matsuoka et al. (2018), and linearly interpolate the QLF parameters ($\log\Phi^*$, M^*, α, β) for other redshifts at $5 < z < 6$. SIMQSO suggests that there are $N_{\rm all} = 485$ quasars brighter than $m_z = 21$ at $5 < z < 6$ in the DES field.

J2037–4537 directly constrains the number of quasar pairs at $z > 5$ with $0.''9 < \Delta d < 3.''0$. The lower boundary of the projected separation corresponds to the spatial resolution of the DES survey. To avoid confusion, we always use r to denote the physical separation of a quasar pair, and use Δd to denote the projected separation. By converting the angular separations to proper distances, we find $f_{\rm pair}[5.3 < \Delta d\,({\rm pkpc}) < 17.7] \geqslant 1/485 = 0.2\%$. As a comparison, the expected number of quasar pairs is 7×10^{-6} if quasars are randomly distributed. We estimate this number by assigning random positions to the quasars in the mock catalog, and counting pairs of mock quasars with $0.''9 < \Delta d < 3.''0$ and $\Delta v < 2000\,{\rm km\,s^{-1}}$, following Hennawi et al. (2006). The clustering signal for $z > 5$ quasars is thus $W_p(0.''9 < \Delta d < 3.''0) \sim 10^5$. Hennawi et al. (2006) measure the quasar correlation function at $1 \lesssim z \lesssim 3$ and $\Delta d \sim 0.1$ pMpc. Extrapolating the correlation function in Hennawi et al. (2006) to small scales gives a clustering signal of $W_p \sim 10^3$. This comparison indicates that close quasar pairs are regulated by processes (likely galaxy mergers) that are different from quasar clustering at larger scales.

In order to make direct comparisons to the simulated pair fractions, we convert $f_{\rm pair}(0.''9 < \Delta d < 3.''0)$ to $f_{\rm pair}(r < 30\,{\rm pkpc})$ as follows. We assume that the small-scale quasar correlation function can be described by a power law, i.e., $\xi(r) = (r/R_0)^{-\gamma}$. Following the analysis in Hennawi et al. (2006) and McGreer et al. (2016), the expected number of quasar pairs with separation $r < R$ can be calculated as

$$N_{\rm pair}(r{<}R) = \frac{1}{2}\sum_j^{N_{\rm all}} \int_0^R n(z_j) \times 4\pi r^2[1 + \xi(r)]dr, \quad (3)$$

where the sum goes through all the mock quasars and $n(z_j)$ is the number density of quasars at redshift z_j that have $m_z < 21$. We use the quasar spectrum template from Vanden Berk et al. (2001) to convert the absolute magnitude M_{1450} to the z-band apparent magnitude. Similarly, the expected number of quasar pairs with projected separation $d_{\rm min} < \Delta d < d_{\rm max}$ is

$$\begin{aligned} &N_{\rm pair}(d_{\rm min}{<}\Delta d < d_{\rm max}) \\ &= \frac{1}{2}\sum_j^{N_{\rm all}} \int_{-\frac{v_{\rm max}}{aH(z_j)}}^{+\frac{v_{\rm max}}{aH(z_j)}} dy \int_{d_{\rm min}}^{d_{\rm max}} dx\, n(z_j) \\ &\quad \times 2\pi x[1 + \xi(\sqrt{y^2 + x^2})], \end{aligned} \quad (4)$$

where $a = (1+z)^{-1}$ is the scale factor, $H(z_j)$ is the Hubble constant at redshift z_j, and $v_{\rm max} = 2000\,{\rm km\,s^{-1}}$ is the maximum velocity difference of the quasar pair. Note that all the quantities in Equations (3) and (4) are in comoving units. We adopt a fiducial power-law index of $\gamma = 2$, which gives a good description of quasar pairs down to a separation of $\lesssim 100$ pkpc (e.g., Shen et al. 2010). At small separations, we have $\xi(r) \gg 1$, and $\gamma = 2$ gives a flat distribution of $\frac{dN_{\rm pair}(r<R)}{R}$, in agreement with the simulated AGN pairs in Rosas-Guevara et al. (2019).

By applying $N_{\rm pair}(0.''9 < \Delta d < 3.''0) > 1$ to the above equations, we get $R_0 > 254h^{-1}$ comoving Mpc (cMpc), $N_{\rm pair}(r < 30\,{\rm pkpc}) > 1.5$, and $f_{\rm pair}(r < 30\,{\rm pkpc}) > 0.3\%$. Figure 4 shows the comparison between our results and the predictions

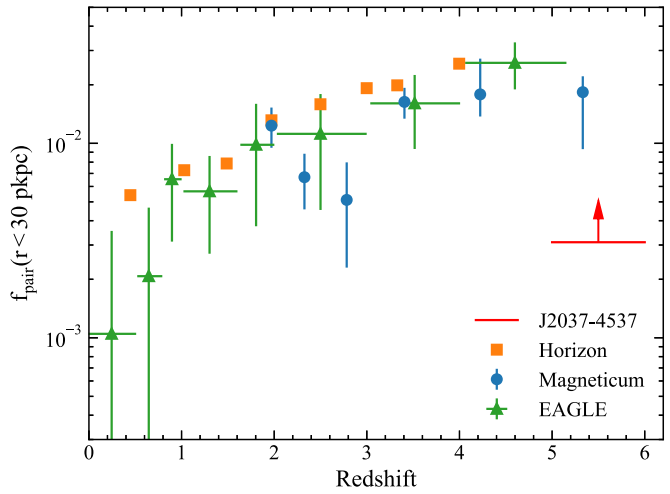

Figure 4. The pair fraction of quasars, $f_{\rm pair}(r < 30$ pkpc). The red line marks the lower limit set by J2037–4537. We also include the predictions of cosmological simulations, which are adapted from Figure 6 in De Rosa et al. (2019). The simulated AGN samples have $L_{\rm bol} > 10^{43}$ erg s^{-1}, and include both obscured and unobscured AGNs. The observed lower limit is several times lower than the simulated sample. Note that the two quasars in J2037–4537 have $L_{\rm bol} \sim 10^{47}$ erg s^{-1} (Table 1). Observations at lower redshift indicate that the pair fraction decreases with AGN luminosity, which could explain the difference between the simulations and the lower limit set by J2037–4537 (see the text for details).

from the cosmological simulations. The lower limit is several times lower than the predicted pair fraction. Note that the simulations count both obscured and unobscured AGNs. Since our survey only targets unobscured type-I quasars, we expect that the observed quasar pair fraction in our survey should be lower than the simulated AGN pair fractions. In addition, the AGN pair fraction depends on the luminosity and the SMBH mass, as discussed in De Rosa et al. (2019). Silverman et al. (2020) give an observed pair fraction of ∼0.26% for $z \lesssim 4$ quasars, and their sample has a luminosity cut ($\log L_{\rm bol} > 45.3$) that is comparable to our survey. Silverman et al. (2020) show that the observed fraction is consistent with a luminosity-matched sample in the cosmological simulations, which indicates that the pair fraction might be lower for luminous AGNs. Current cosmological simulations do not have sufficient volumes to produce a quasar pair like J2037–4537 at $z > 5$. Future simulations with larger volumes will enable direct comparisons with observations and provide unique constraints on the SMBH evolution models at high redshift.

3.2. The Triggering Mechanism of the Quasar Pair

The tangential separation between the two quasars in J2037–4537 is 7.3 kpc, and the spectra suggest a redshift difference of $\Delta z \lesssim 0.01$. As such, this quasar pair must reside in a galaxy merger. Although current data cannot rule out the possibility that the two quasars are triggered independently and coincidentally before the merging event, we argue that J2037–4537 is likely triggered by the galaxy merger. This is because the correlation length indicated by J2037–4537 ($R_0 > 254h^{-1}$ cMpc) is much larger than the correlation length of $z \sim 5$ quasars ($R_0 \sim 20h^{-1}$ cMpc; e.g., McGreer et al. 2016). The significant difference in R_0 at large and small scales indicates that close quasar pairs and quasar pairs with separation $\gtrsim$100 pkpc might have different origins. The former are more likely results of galaxy mergers, while the latter are related to structure formation at sub-Mpc scales. Connor et al. (2019) report a quasar/galaxy merger system at $z = 6.23$, in which the companion galaxy contains a candidate of a highly obscured X-ray AGN.

The observational features of J2037–4537 are consistent with merger-triggered quasar pairs in hydrodynamical simulations. Capelo et al. (2017) explore the factors that control the emergence of AGN pairs in galaxy mergers, and conclude that close quasar pairs usually appear in galaxy mergers with SMBH mass ratios close to one and separations less than 10 pkpc. It is thus plausible that the two quasars are triggered by the merging process. Future observations (likely with ALMA or the James Webb Space Telescope) will reveal more details of the gas kinematics and will allow us to investigate how the gas feeds the SMBHs in this system. Besides, we notice that the two quasars show similar profiles for a few broad emission lines (e.g., the Lyα, N V, O I, and Si IV lines). If J2037–4537 is a physical quasar pair, these similarities might be causally connected to the physical association of the two quasars and encode critical information about how the quasar activities are triggered.

4. Summary

We report the discovery of a close quasar pair candidate at $z = 5.66$, J2037–4537, which has a projected separation of 1.″24 (7.3 kpc). The ground-based spectroscopy shows that the resolved two objects are two quasars at the same redshift, and the high-resolution HST imaging does not detect the foreground lensing galaxy. Given the features in the spectra and the high-resolution images, it is highly unlikely that J2037–4537 is a lensed quasar. J2037–4537 sets the first constraint on the pair fraction of quasars at $5 < z < 6$, $f_{\rm pair}(r < 30\,{\rm pkpc}) > 0.3\%$. Future observations of the gas kinematics in J2037–4537 will reveal more information about the triggering mechanism of the quasar pair.

We thank the referee and the editor for their valuable comments. This research is based on observations made with the NASA/ESA Hubble Space Telescope obtained from the Space Telescope Science Institute, which is operated by the Association of Universities for Research in Astronomy, Inc., under NASA contract NAS 526555. These observations are associated with program GO-16507. Some of the data presented in this paper were obtained from the Mikulski Archive for Space Telescopes (MAST) at the Space Telescope Science Institute. The specific observations analyzed can be accessed via 10.17909/t9-gw19-6w51. This paper includes data gathered with the 6.5 meter Magellan Telescopes located at Las Campanas Observatory, Chile. M.Y., X.F., and J.Y. acknowledge support by NSF grants AST 19-08284. M.Y. and X.F. acknowledge support by HST-GO-16507 grant from the Space Telescope Science Institute. F.W. is thankful for the support provided by NASA through the NASA Hubble Fellowship grant #HST-HF2-51448.001-A awarded by the Space Telescope Science Institute, which is operated by the Association of Universities for Research in Astronomy, Incorporated, under NASA contract NAS5-26555.

Facilities: HST, Magellan/Clay, Magellan/Baade.

ORCID iDs

Minghao Yue https://orcid.org/0000-0002-5367-8021
Xiaohui Fan https://orcid.org/0000-0003-3310-0131
Jinyi Yang https://orcid.org/0000-0001-5287-4242
Feige Wang https://orcid.org/0000-0002-7633-431X

References

Abbott, T. M. C., Abdalla, F. B., Allam, S., et al. 2018, ApJS, 239, 18
Capelo, P. R., Dotti, M., Volonteri, M., et al. 2017, MNRAS, 469, 4437
Capelo, P. R., Volonteri, M., Dotti, M., et al. 2015, MNRAS, 447, 2123
Cole, S., Lacey, C. G., Baugh, C. M., & Frenk, C. S. 2000, MNRAS, 319, 168
Connor, T., Bañados, E., & Stern, D. 2019, ApJ, 887, 171
De Rosa, A., Vignali, C., Bogdanović, T., et al. 2019, NewAR, 86, 101525
Decarli, R., Walter, F., Venemans, B. P., et al. 2018, ApJ, 854, 97
Di Mascia, F., Gallerani, S., Behrens, C., et al. 2021, MNRAS, 503, 2349
Di Matteo, T., Springel, V., & Hernquist, L. 2005, Natur, 433, 604
Dubois, Y., Pichon, C., Welker, C., et al. 2014, MNRAS, 444, 1453
Faber, S. M., Willmer, C. N. A., Wolf, C., et al. 2007, ApJ, 665, 265
Hennawi, J. F., Myers, A. D., Shen, Y., et al. 2010, ApJ, 719, 1672
Hennawi, J. F., Strauss, M. A., Oguri, M., et al. 2006, AJ, 131, 1
Hilbert, S., White, S. D. M., Hartlap, J., & Schneider, P. 2008, MNRAS, 386, 1845
Jee, M. J., Blakeslee, J. P., Sirianni, M., et al. 2007, PASP, 119, 1403
Kim, Y., Im, M., Jeon, Y., et al. 2020, ApJ, 904, 111
Kulkarni, G., Worseck, G., & Hennawi, J. F. 2019, MNRAS, 488, 1035
Mason, C. A., Treu, T., Schmidt, K. B., et al. 2015, ApJ, 805, 79
Matsuoka, Y., Strauss, M. A., Kashikawa, N., et al. 2018, ApJ, 869, 150
McGreer, I. D., Eftekharzadeh, S., Myers, A. D., & Fan, X. 2016, AJ, 151, 61
McGreer, I. D., Jiang, L., Fan, X., et al. 2013, ApJ, 768, 105
Onoue, M., Kashikawa, N., Uchiyama, H., et al. 2018, PASJ, 70, S31
Peng, C. Y., Ho, L. C., Impey, C. D., & Rix, H.-W. 2002, AJ, 124, 266
Prochaska, J. X., Hennawi, J. F., Westfall, K. B., et al. 2020, JOSS, 5, 2308
Rorai, A., Hennawi, J. F., Oñorbe, J., et al. 2017, Sci, 356, 418
Rosas-Guevara, Y. M., Bower, R. G., McAlpine, S., Bonoli, S., & Tissera, P. B. 2019, MNRAS, 483, 2712
Ross, N. P., McGreer, I. D., White, M., et al. 2013, ApJ, 773, 14
Runnoe, J. C., Brotherton, M. S., & Shang, Z. 2012, MNRAS, 422, 478
Schaye, J., Crain, R. A., Bower, R. G., et al. 2015, MNRAS, 446, 521
Shen, Y., Chen, Y.-C., Hwang, H.-C., et al. 2021, NatAs, 5, 569
Shen, Y., Hennawi, J. F., Shankar, F., et al. 2010, ApJ, 719, 1693
Silverman, J. D., Tang, S., Lee, K.-G., et al. 2020, ApJ, 899, 154
Sluse, D., Hutsemékers, D., Courbin, F., Meylan, G., & Wambsganss, J. 2012, A&A, 544, A62
Steinborn, L. K., Dolag, K., Comerford, J. M., et al. 2016, MNRAS, 458, 1013
Tang, S., Silverman, J. D., Ding, X., et al. 2021, arXiv:2105.10163
Vanden Berk, D. E., Richards, G. T., Bauer, A., et al. 2001, AJ, 122, 549
Vestergaard, M., & Peterson, B. M. 2006, ApJ, 641, 689
Volonteri, M., Dubois, Y., Pichon, C., & Devriendt, J. 2016, MNRAS, 460, 2979
Wang, F., Wu, X.-B., Fan, X., et al. 2016, ApJ, 819, 24
Wyithe, J. S. B., Yan, H., Windhorst, R. A., & Mao, S. 2011, Natur, 469, 181
Yang, J., Fan, X., Wu, X.-B., et al. 2017, AJ, 153, 184
Yang, J., Wang, F., Fan, X., et al. 2019, ApJ, 871, 199